

## 光学学报

## 基于空间光调制器的远场超分辨光场构建

李新羽<sup>1</sup>, 黄宇文<sup>2</sup>, 赵昶栋<sup>1</sup>, 邹依洋<sup>2</sup>, 李占锋<sup>1</sup>, 尚丽平<sup>2,3</sup>, 邓琥<sup>2</sup>, 王志翔<sup>2\*</sup><sup>1</sup>西南科技大学制造科学与工程学院, 四川 绵阳 621010;<sup>2</sup>西南科技大学信息工程学院, 四川 绵阳 621010;<sup>3</sup>西南科技大学极端条件物质特性联合实验室, 四川 绵阳 621010

**摘要** 针对传统聚焦器件受到衍射极限的限制问题,提出了一种基于空间光调制器的远场超分辨聚焦光场构建方法,采用光学超振荡原理,结合二进制粒子群算法和角谱衍射理论,针对波长 $\lambda=632.8$  nm的圆偏振光,通过在空间光调制器液晶屏上加载超振荡相位掩模的方式,得到了焦距 $f=300000\lambda(18984\ \mu\text{m})$ 、半径 $R=4000\lambda(2531.2\ \mu\text{m})$ 的远场超分辨聚焦器件,并利用物镜结合互补金属氧化物半导体(CMOS)相机的测量方案对其进行特征参数表征。实验结果表明:该器件通过对入射光场的相位调控,生成了纵向半峰全宽为6.029 mm的针状聚焦光场;聚焦焦斑目标焦距位置处的横向半峰全宽为22.384  $\mu\text{m}$ ,小于衍射极限23.732  $\mu\text{m}$ ,实现了远场超分辨聚焦。该器件具有结构尺寸小、无需复杂加工等特点,在光学显微、光学遥感等领域中具有应用潜力。

**关键词** 物理光学; 空间光调制器; 光学超振荡; 远场超分辨聚焦; 角谱衍射; 光场测量

中图分类号 O436

文献标志码 A

DOI: 10.3788/AOS240552

## 1 引言

传统聚焦器件受到阿贝衍射极限的限制,即空间分辨率不能超过其理论最小值 $0.5\lambda/NA$ <sup>[1]</sup>,其中 $\lambda$ 是工作波长, $NA$ 是数值孔径。突破衍射极限(DL),从而构建超分辨聚焦光场,对光学显微<sup>[2]</sup>、光学遥感<sup>[3]</sup>、亚波长光刻<sup>[4]</sup>、超高密度数据存储<sup>[5]</sup>等相关领域具有重要的意义。现有的突破衍射极限聚焦的方法,如光瞳滤波法<sup>[6]</sup>、表面等离子共振法<sup>[7,8]</sup>、负折射超构透镜<sup>[9]</sup>等,需要在近场环境下工作,无法满足光学意义上远场超分辨成像需求。

光学超振荡<sup>[10]</sup>是指空间频率较低的光场相干叠加,并在空间局域形成快速振荡光场的现象。该局域振荡频率可以远大于光场最高空间频率,并在局域空间形成最小特征尺寸小于光学衍射极限的光场分布。通过合理调制入射光的波前,传输光场在远场焦平面内发生干涉,理论上可以产生任意小的超分辨聚焦焦斑<sup>[11]</sup>。

近年来,基于光学超振荡原理,研究人员在超分辨光学透镜领域开展了大量研究<sup>[12]</sup>。2020年,Zhang等<sup>[13]</sup>设计了可在一定视场范围内工作的大数值孔径超振荡透镜,针对波长为632.8 nm的线偏振光,通过

$\text{SiO}_2$ 基底上不同旋向的非晶硅纳米矩形块实现所需的超振荡相位调制,优化出的超振荡透镜为32阶相位分布,实验结果表明,在焦距 $60\lambda$ 处实现了约0.874倍阿贝衍射极限分辨力的超振荡聚焦;2023年,Zheng等<sup>[14]</sup>针对工作波长为632.8 nm的偏振光设计了一种复合超振荡透镜,由 $\text{SiO}_2$ 基底和氮化硅圆环构成内透镜和外透镜,分别用来压缩焦点尺寸和抑制旁瓣,在 $1500\lambda$ 的远场范围内可以达到 $0.315\lambda/NA$ 的分辨率,同时旁瓣比低至0.89%。上述超振荡透镜在实验上实现了远场超分辨聚焦,其光场调控依赖于精密的纳米加工技术。由于其制造成本较高且复杂度较大,该器件限制在较小尺寸范围内。

空间光调制器(SLM)作为一种可调制光波的光场分布的元件,常用于光场调控研究,如将高斯光束整形为平顶光束<sup>[15]</sup>、生成自动聚焦的旋转光束<sup>[16]</sup>、生成相位型光栅产生点阵结构光<sup>[17]</sup>等。2019年,Xu等<sup>[18]</sup>利用空间光调制器提出一种逐步补零算法以生成二元相位调制元件,结合显微镜物镜聚焦,在线性贝塞尔-高斯光束入射下产生了超分辨空心光斑,其半峰全宽(FWHM)为0.967倍的阿贝衍射极限;2022年,夏小兰等<sup>[19]</sup>利用两个空间光调制器和环形光衰减片分别对径向和角向两种偏振光场的波前进行调控,将两光束按

收稿日期: 2024-01-23; 修回日期: 2024-03-02; 录用日期: 2024-03-18; 网络首发日期: 2024-04-12

基金项目: 国家自然科学基金(62105271)、四川省科技厅支撑计划(2020YJ0160)、西安近代化工研究所开放基金(SYJJ20210411)、西南科技大学博士基金(19zx7160)

通信作者: \*zxwu@swust.edu.cn

照一定的强度比例叠加,合成准球形多焦点阵列,焦点的纵向和横向的 FWHM 均为 0.745 倍的阿贝衍射极限。上述研究利用空间光调制器得到了超分辨光斑,其实现超分辨聚焦过程依赖于空间光调制器和其他光学器件,存在光路调节复杂、光学器件中心同轴等问题。

本文提出了一种基于空间光调制器生成远场超分辨聚焦光场的方法,采用超振荡原理,设计了远场超分辨聚焦器件,该器件在  $0\sim 2\pi$  范围内采用 8 值相位调控。利用物镜和互补金属氧化物半导体 (COMS) 相机对超分辨聚焦光场进行测量,结果表明,在波长  $\lambda=632.8\text{ nm}$  的圆偏振光入射下,目标焦距位置 ( $f=300000\lambda$ ) 处产生了峰值 FWHM 为  $22.384\text{ }\mu\text{m}$  的聚焦焦斑,小于阿贝衍射极限 ( $0.5\lambda/NA, 23.732\text{ }\mu\text{m}$ ),实现了远场超分辨聚焦。该研究在高密度磁光存储、超分辨光学成像、纳米光刻与粒子操作等领域中具有广泛的应用前景。

## 2 远场超分辨聚焦器件设计方法及结果

图 1 是在圆偏振光入射下,远场超分辨聚焦器件聚焦示意图。圆偏振光入射到空间光调制器液晶屏上,由相位掩模调控后反射,在焦距  $f$  处进行干涉,形成超分辨聚焦光场。采用二进制粒子群算法<sup>[20]</sup>,并结

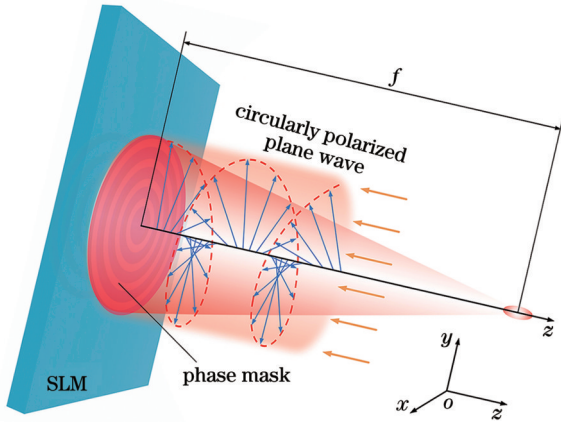


图 1 基于空间光调制器的远场超分辨聚焦工作原理

Fig. 1 Working principle of far-field super-resolution focusing based on spatial light modulator

合角谱衍射理论<sup>[21]</sup>,对远场超分辨聚焦器件相位调控掩模进行优化设计,并利用空间光调制器的相位调控功能调节所设计器件相位分布,在目标焦距处形成聚焦焦斑。

光学超振荡是指由空间频率较低的光场相干叠加,在空间形成局域振荡频率可以远大于光场最高空间频率的现象,可在局域空间形成最小特征尺寸小于光学衍射极限的光场分布。函数  $F(x)$  可由  $N_0$  个谐波线性叠加而成<sup>[4]</sup>,这些谐波分解为一系列传播方向不同的相干平面波,这些平面波相干叠加形成衍射光场  $F(x)$ ,具体表达式为

$$F(x) = A \exp(i\varphi) = \sum_{n=0}^{n=N_0} a_n \exp(i2n\pi x) \quad (1)$$

式中:  $A$  为衍射光场的振幅;  $\varphi$  为衍射光场的相位;  $a_n$  为复振幅;  $i$  为虚数单位。第  $n$  个平面波在  $x$  轴方向的空间频率为  $k_x = 2\pi nx$ , 最高次谐波对应的空间频率为  $2\pi N_0 x$ 。因此,可以对复振幅  $a_n$  进行合理优化设计,实现衍射光场  $F(x)$  空间局域快速振荡 (远大于最高空间频率),进而实现远场超分辨光场构建<sup>[22]</sup>。

二进制粒子群算法优化设计超振荡掩模流程图如图 2 所示,具体步骤:输入器件参数,包括波长  $\lambda$ 、焦距  $f$ 、半径  $R$  等;进一步设置入射光场为圆偏振光、器件为 8 值相位调控器件、目标光场参数 (适应度函数)、粒子群算法参数 (其中  $c_1$  和  $c_2$  分别是粒子群优化算法里的个体学习因子和群体学习因子);随机初始化每个粒子即初始化掩模的相位结构,视为个体历史最优位置,以及整个粒子群的全局历史最优位置;利用角谱衍射计算公式,计算聚焦器件的衍射光场,进而获得目标位置上聚焦焦斑的适应度值;判断适应度值是否满足,若不满足,使每个粒子 (器件) 向全局最优位置靠近,若满足,则输出掩模最佳相位和对应的特征参数,结束优化设计。

优化过程中的衍射光场由角谱衍射理论计算得到,将光场看作是许多不同方向传播的单色平面波分量的线性组合,每一平面波分量的相对振幅和相位取决于相应的角谱。假设入射光场为  $U(x, y, 0)$ , 位于  $z=0$  处,依据傅里叶变换和傅里叶逆变换可计算得到  $(x, y, z)$  处的光场  $U(x, y, z)$ ,具体过程为

$$\begin{cases} A\left(\frac{\alpha}{\lambda}, \frac{\beta}{\lambda}, 0\right) = \int_{-\infty}^{+\infty} \int_{-\infty}^{+\infty} U(x, y, 0) \exp\left[-i2\pi\left(\frac{\alpha}{\lambda}x + \frac{\beta}{\lambda}y\right)\right] dx dy \\ A\left(\frac{\alpha}{\lambda}, \frac{\beta}{\lambda}, z\right) = A\left(\frac{\alpha}{\lambda}, \frac{\beta}{\lambda}, 0\right) \exp\left[\frac{i2\pi}{\lambda} \sqrt{1 - (\alpha^2 + \beta^2)} \times z\right] \\ U(x, y, z) = \int_{-\infty}^{+\infty} \int_{-\infty}^{+\infty} A\left(\frac{\alpha}{\lambda}, \frac{\beta}{\lambda}, z\right) \exp\left[-i2\pi\left(\frac{\alpha}{\lambda}x + \frac{\beta}{\lambda}y\right)\right] d\frac{\alpha}{\lambda} d\frac{\beta}{\lambda} \end{cases}, \quad (2)$$

式中:  $A(\alpha/\lambda, \beta/\lambda, 0)$  和  $A(\alpha/\lambda, \beta/\lambda, z)$  分别为反射平面和聚焦平面的角谱;  $\alpha$  和  $\beta$  为方向余弦。

针对工作波长为  $\lambda=632.8\text{ nm}$  的圆偏振光,设定远场超分辨聚焦器件焦距和半径分别为  $f=300000\lambda$

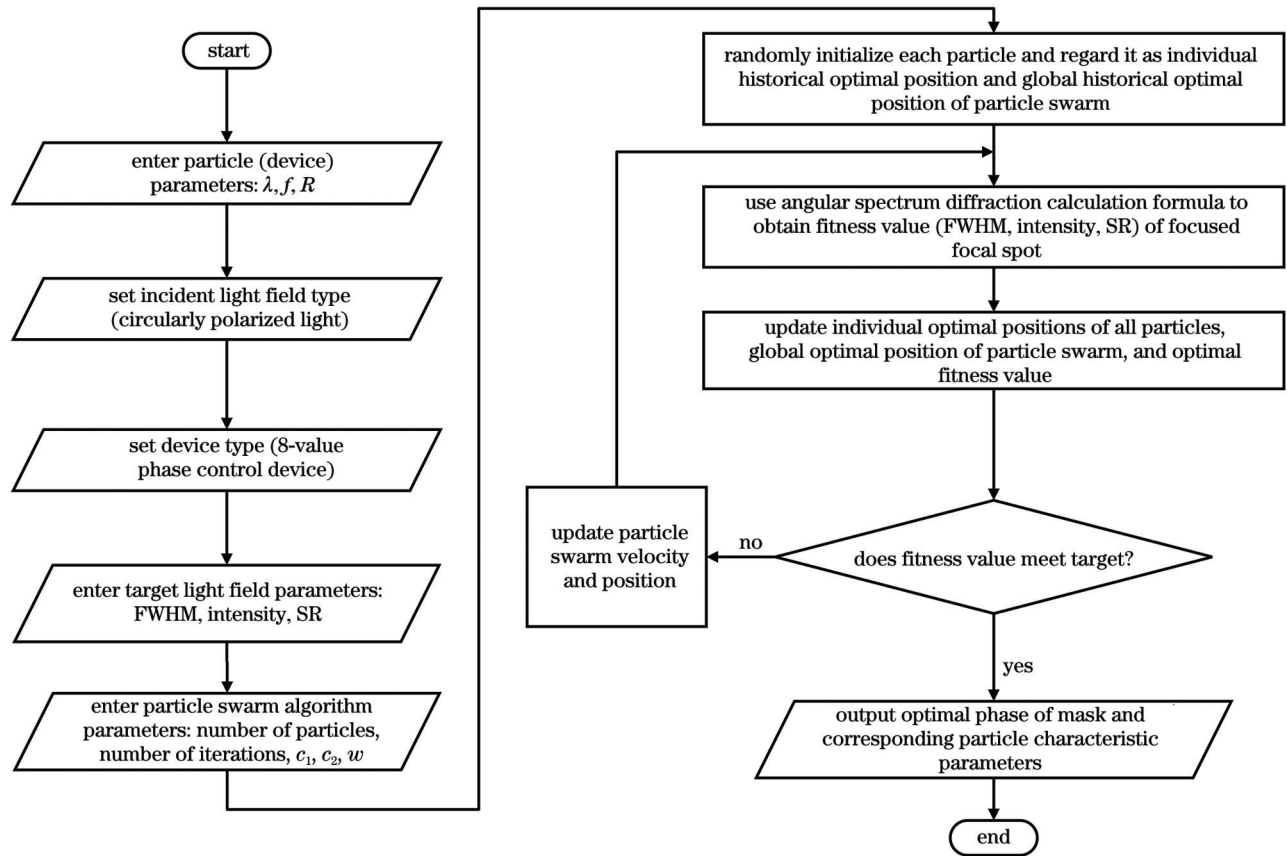


图 2 二进制粒子群算法优化设计超振荡掩模流程图

Fig. 2 Flowchart of binary particle swarm algorithm for optimal design of super-oscillatory mask

(18984  $\mu\text{m}$ ) 和  $R=4000\lambda$  (2531.2  $\mu\text{m}$ ), 数值孔径为 0.013, 相应的阿贝衍射极限为  $37.503\lambda$  (23.732  $\mu\text{m}$ )。所设计器件采用 8 值相位调控 ( $0, \pi/4, \pi/2, \dots, 7\pi/4$ ), 利用二进制粒子群算法, 对器件的二维相位分布进行了优化设计。该器件由一系列同心环带组成, 每个环带的宽度相等, 即  $w=8 \mu\text{m}$ , 与后续实验中使用

的空间光调制器像素尺寸一致。第  $i$  个环带所对应的相位为同一相位  $\varphi_i$  ( $i=1, 2, 3, \dots, N$ )。为了在实验中实现所优化设计的相位掩模, 需要计算出每个环带相位  $\varphi_i$ 。相位掩模所对应的灰度图像如图 3(a) 所示, 该相位掩模由  $N=316$  个同心环带组成。图 3(b) 显示了优化后的掩模相位分布, 横坐标为每个环带

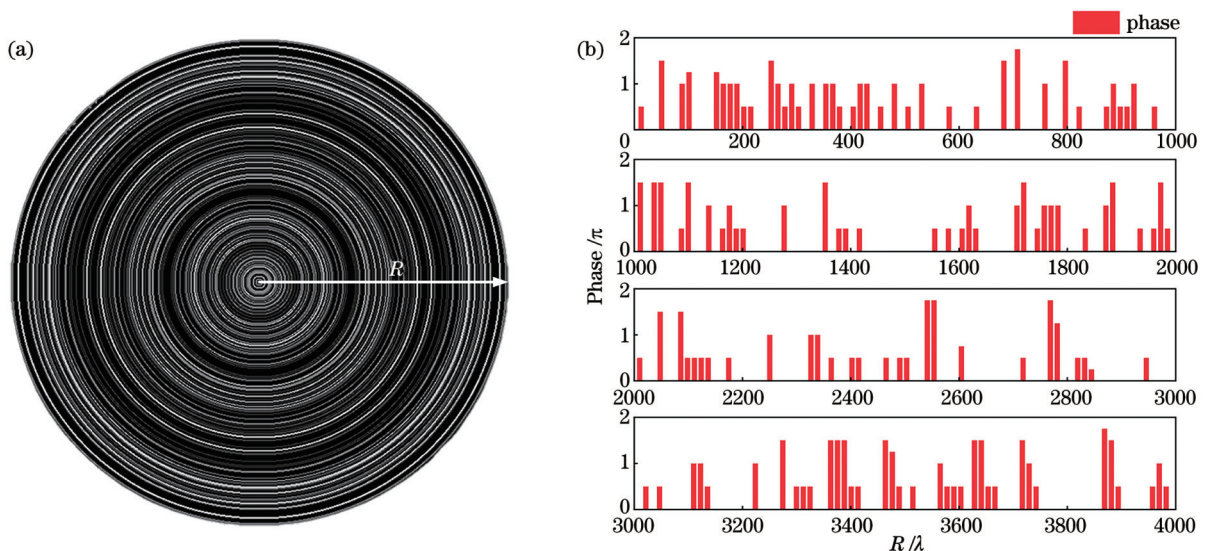


图 3 超振荡掩模的相位调控分布。(a) 超振荡掩模相位分布灰度图; (b) 沿半径方向相位分布

Fig. 3 Phase modulation distribution of super-oscillatory mask. (a) Grayscale image of phase distribution of super-oscillatory mask; (b) phase distribution along radial direction

中心所在的径向位置,柱状图给出了每个环带所对应的相位。

图 4(a)给出了所设计器件沿光轴  $Z=180.00$  mm 到  $Z=200.00$  mm 范围内,在圆偏振光入射条件下传播平面上计算得到的聚焦光场分布,在设计焦距处,出现了较为明亮的聚焦焦斑,在其周围存在一些较为微弱的旁瓣,图中虚线为焦平面所在位置。聚焦焦斑沿传播方向的峰值强度 Intensity、横向 FWHM、旁瓣比(SR)如图 4(b)所示,短划线对应衍射

极限  $0.5\lambda/NA$ ,点线对应瑞利判据(RL)<sup>[23]</sup> $0.61/\lambda NA$ ,聚焦焦斑附近绝大区域的横向 FWHM 小于衍射极限,远小于瑞利判据,焦斑沿传播方向的 FWHM ( $x_{FWHM,z}$ )为  $6.017$  mm。图 4(c)、(d)给出了  $Z=189.84$  mm 处 XY 平面上获得的二维强度分布和强度分布曲线,可以看出,强度分布呈现以光轴为中心的清晰焦斑,周围存在一些小旁瓣,焦斑横向 FWHM ( $x_{FWHM,x}$ )为  $34.375\lambda$  ( $21.753 \mu\text{m}$ ),小于衍射极限  $23.732 \mu\text{m}$ 。

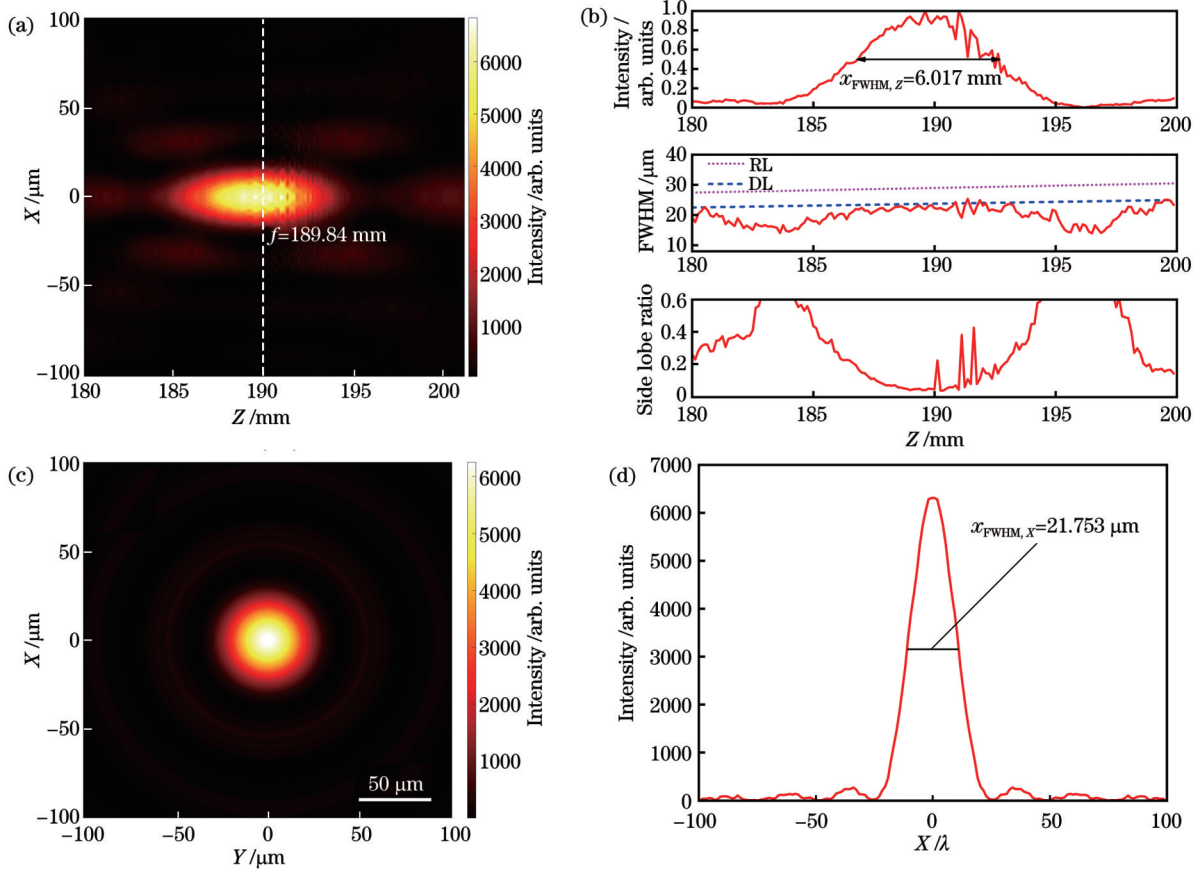


图 4 理论设计结果。(a)传播平面光场强度;(b)传播方向峰值强度、横向 FWHM 和旁瓣比率曲线图;(c)焦平面光场强度;(d)通过焦斑中心沿半径方向上光场强度曲线图

Fig. 4 Theoretical design results. (a) Propagation plane optical field intensity; (b) propagation direction peak intensity, transverse FWHM and side lobe ratio curves; (c) focal plane optical field intensity; (d) field intensity curve along radius through center of focal spot

### 3 实验结果及讨论

为了验证所设计器件的聚焦性能,设计并搭建了远场超分辨聚焦光场构建及测量系统,如图 5 所示,采用物镜结合 CMOS 相机,对超分辨聚焦光场特征参数进行测量。光源为氦氖激光器(Thorlabs,HNL100L),波长为  $632.8$  nm,光束直径为  $0.68$  mm。采用自由空间光隔离器(Thorlabs,IO-3D-633-VLP)对器件反射的光束进行隔离,防止对激光器造成损伤,同时提高光束质量。由线偏振片(大恒光电,GCL-050003)和四分之一波片(大恒光电,GCL-060624)生成圆偏振光。为

了在聚焦器件范围内获得较为均匀的人射光场,采用扩束器(Thorlabs,GBE20-A-20X)对偏振光进行扩束。实验使用的空间光调制器(HOLOEYE PLUTO-NIR-015)是纯相位反射式空间光调制器,像素间距为  $8 \mu\text{m}$ ,分辨率为  $1920 \text{ pixel} \times 1080 \text{ pixel}$ ,相位级别为 256;空间光调制器液晶屏上加载的超振荡掩模对入射光场进行相位调制,在焦距  $f$  处进行干涉,形成远场超分辨聚焦光场;在焦距  $f$  处使用前置物镜的相机(Basler,acA3800-14 μm)测量聚焦光场,通过移动电控位移台(Thorlabs,NRT150/M)获取不同位置处的二维光场分布,再通过图像处理算法提取

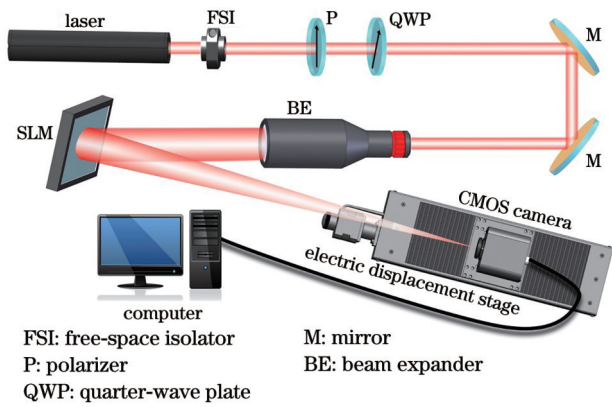


图 5 基于空间光调制器的远场超分辨聚焦光场构建和测量平台示意图

Fig. 5 Schematic diagram of the platform for far-field super-resolution focusing optical field construction and measurement platform based on spatial light modulator

聚集焦斑关键聚焦参数,得到聚焦光场的三维强度分布。

实验中,对  $Z=185.00\text{ mm}$  至  $Z=195.00\text{ mm}$  范围

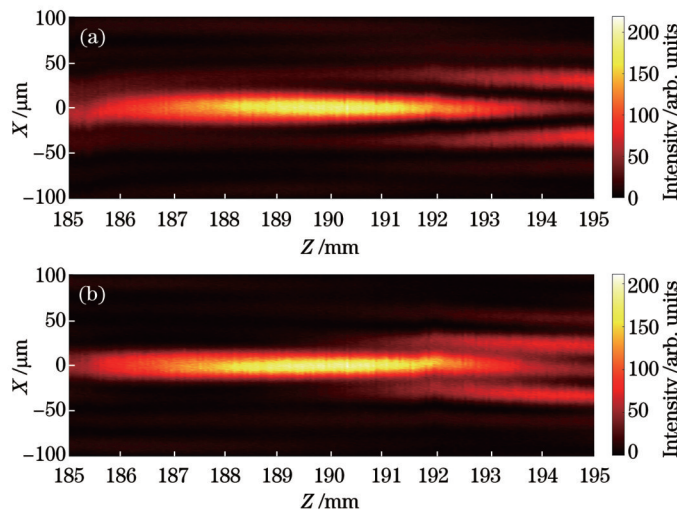
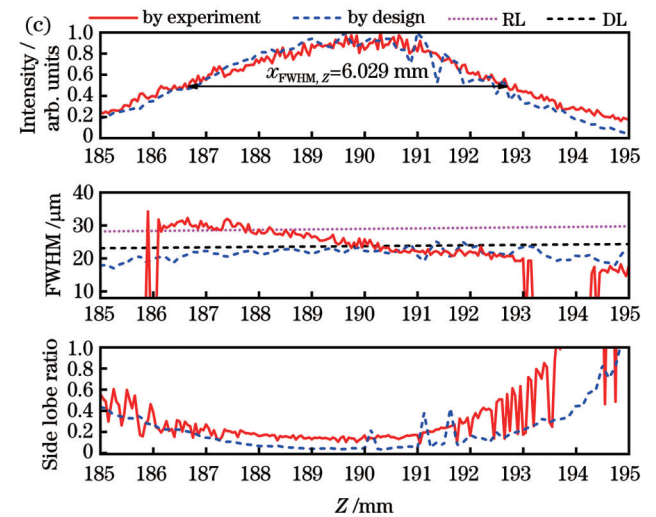


图 6 传播方向实验测试结果。(a) XZ 平面光场强度;(b) YZ 平面光场强度;(c) XZ 平面峰值强度、横向 FWHM 和旁瓣比曲线  
Fig. 6 Experimental test results of propagation direction. (a) XZ plane optical field intensity; (b) YZ plane optical field intensity; (c) peak intensity, transverse FWHM and side lobe ratio curves

聚焦光场沿传播方向 FWHM 范围为  $186.668\sim 192.697\text{ mm}$ ,如图 7(a)所示,在焦距附近产生了针状结构的聚焦光场,并存在一些稍弱的旁瓣。图 7(b)~(e)分别显示了  $Z=186.50, 188.50, 190.50, 192.50\text{ mm}$  处的 XY 平面光场强度分布,平面中心出现明亮焦斑;图 7(a)中的虚线为沿径向穿过焦斑中心的切割线,图 7(f)~(i)为沿虚线绘制的 X 轴方向(实线)和 Y 轴(点线)方向强度分布曲线,X 轴方向对应的 FWHM 分别为  $27.604, 27.610, 21.449, 19.919\text{ }\mu\text{m}$ ;Y 轴方向对应的 FWHM ( $x_{\text{FWHM},y}$ ) 分别为  $30.161, 23.830, 19.404, 24.731\text{ }\mu\text{m}$ ;对 XY 平面作 8 条截线,得到的平均 FWHM ( $x_{\text{FWHM},a}$ ) 分别为  $27.355, 25.426, 20.757,$

内的光场进行了扫描测试,扫描步长  $\Delta Z=0.05\text{ mm}$ 。图 6(a)和图 6(b)分别给出了 XZ 平面和 YZ 平面的光场强度分布,可以看出 XZ 平面和 YZ 平面的聚焦光场周围存在强度较弱的旁瓣。图 6(c)给出了聚焦焦斑沿传播方向上的峰值强度、横向 FWHM、旁瓣比的分布曲线,实线为实验结果,虚线为设计结果,短划线为衍射极限,点线为瑞利判据。由图 6(c)可知,设计和实验所得到的光场强度相吻合,聚焦焦斑目标焦距位置处的横向 FWHM 为  $22.384\text{ }\mu\text{m}$ ,小于衍射极限  $23.732\text{ }\mu\text{m}$ ,实现了远场超分辨聚焦;沿传播方向上峰值 FWHM 为  $6.029\text{ mm}$ ,形成了一个光针形状的聚焦光场;测量的横向 FWHM 在  $Z=189.50\text{ mm}$  处突破衍射极限,并且之后光场的 FWHM 均小于衍射极限;在  $Z=187.00\text{ mm}$  至  $Z=191.00\text{ mm}$  范围内,旁瓣比小于 23%。对比结果表明,所设计聚焦器件在保证较小旁瓣比的同时,实现了远场超分辨聚焦;理论结果和实验结果存在细微差异,这主要归因于入射光小角度倾斜入射、空间光调制器相位调控误差和光路调节过程中存在的细微偏差。



$21.769\text{ }\mu\text{m}$ 。在不改变其他条件的情况下,将入射光场设置为线偏振光,对聚焦光场进行测量,结果显示聚焦光场 XZ 平面和 YZ 平面焦距处横向 FWHM 分别为  $23.716\text{ }\mu\text{m}$  和  $23.372\text{ }\mu\text{m}$ ,略小于衍射极限  $23.732\text{ }\mu\text{m}$ ,实验结果表明,当入射光为线偏振光情况下,设计结果仍然适用。

## 4 结 论

面向传统聚焦器件受到衍射极限制约的问题,基于光学超振荡原理,提出了一种 8 值相位调控的远场超分辨聚焦光场构建方法,并采用二进制粒子群算法

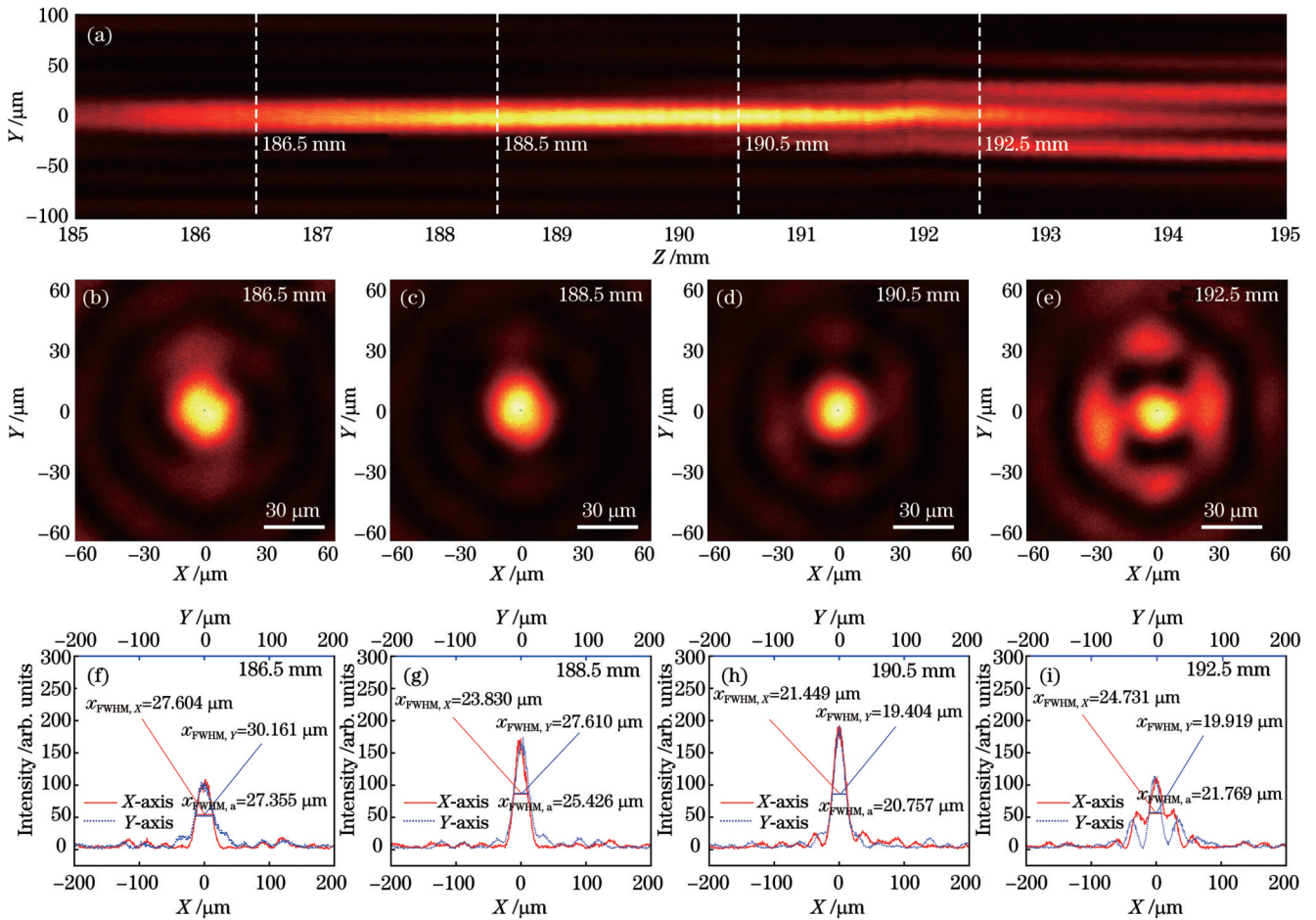


图 7 光场截面实验结果。(a) XZ 平面光场强度;(b)~(e) Z 为 186.50、188.50、190.50、192.50 mm 处的 XY 平面光场强度;(f)~(i) Z 为 186.50、188.50、190.50、192.50 mm 处的强度分布曲线

Fig. 7 Experimental results of optical field cross section. (a) Intensity of light field in XZ plane; (b)–(e) intensity of light field in XY plane at Z of 186.50, 188.50, 190.50, 192.50 mm; (f)–(i) intensity distribution curves at Z of 186.50, 188.50, 190.50, 192.50 mm

和角谱衍射理论,针对波长为 632.8 nm 的圆偏振光,通过在空间光调制器液晶屏上加载超振荡相位掩模的方式,设计了焦距  $f=300000\lambda$  的远场超分辨聚焦器件,同时利用物镜结合 CMOS 相机在实验上测量了光场的特征参数。实验结果表明:该器件通过对入射光场的相位调控,生成了纵向 FWHM 为 6.029 mm 的针状聚焦光场;聚焦焦斑目标焦距位置处的横向 FWHM 为 22.384 μm,小于衍射极限 23.732 μm,实现了远场超分辨聚焦。相对于现有超振荡器件,所设计的远场超分辨聚焦器件具有操作便捷、无需复杂加工等特点,可以应用于可见光波段并可拓展到其他光学波段,为光学显微、光学成像及其他光学应用提供核心聚焦器件。

参 考 文 献

[1] Abbe E. Beiträge zur Theorie des Mikroskops und der mikroskopischen Wahrnehmung[J]. Archiv Für Mikroskopische Anatomie, 1873, 9(1): 413-468.  
 [2] Wang S Y, Zhang D X, Zhang H J, et al. Super-resolution optical microscopy based on scannable cantilever-combined microsphere[J]. Microscopy Research and Technique, 2015, 78

(12): 1128-1132.

[3] Wang P J, Bayram B, Sertel E. A comprehensive review on deep learning based remote sensing image super-resolution methods[J]. Earth Science Reviews, 2022, 232: 104110.  
 [4] Rogers E T F, Zheludev N I. Optical super-oscillations: sub-wavelength light focusing and super-resolution imaging[J]. Journal of Optics, 2013, 15(9): 094008.  
 [5] Ruan H. Mechanism of three-dimensional dual-beam super-resolution optical storage technology[C]//proceedings of the Information Storage System and Technology 2019, November 11–14, 2019, Wuhan, China. Washington, DC: OSA, 2019: ITu2D.4.  
 [6] Li S, Qiu L, Wang Y, et al. Super-resolution radially polarized pupil-filtering confocal Raman spectroscopy technology[J]. Measurement Science and Technology, 2019, 31(3): 035903.  
 [7] 陈燕坤, 韩伟华, 李小明, 等. 突破衍射极限的表面等离子体微元[J]. 光电技术应用, 2011, 26(4): 39-44.  
 Chen Y K, Han W H, Li X M, et al. Surface plasmonics polaritons beyond diffraction limit[J]. Electro-Optic Technology Application, 2011, 26(4): 39-44.  
 [8] Shoup D N, Scarpitti B T, Schultz Z D. A wide-field imaging approach for simultaneous super-resolution surface-enhanced Raman scattering bioimaging and spectroscopy[J]. ACS Measurement Science Au, 2022, 2(4): 332-341.  
 [9] Zhao H X, Xie J L, Liu J J. An approximate theoretical explanation for super-resolution imaging of two-dimensional photonic quasi-crystal flat lens[J]. Applied Physics Express,

- 2020, 13(2): 022007.
- [10] Rogers Edward T F, Jari L, Tapashree R, et al. A super-oscillation lens optical microscope for subwavelength imaging[J]. *Nature Materials*, 2012, 11(5): 432-435.
- [11] Huang F M, Zheludev N I. Super-resolution without evanescent waves[J]. *Nano Letters*, 2009, 9(3): 1249-1254.
- [12] 郑鹏程, 谢向生, 梁浩文, 等. 面向光信息存储的小尺寸光场研究进展[J]. *中国激光*, 2023, 50(18): 1813012.  
Zheng P C, Xie X S, Liang H W, et al. Small size optical field advancements for optical information storage[J]. *Chinese Journal of Lasers*, 2023, 50(18): 1813012.
- [13] Zhang Q, Dong F L, Li H X, et al. High-numerical-aperture dielectric metalens for super-resolution focusing of oblique incident light[J]. *Advanced Optical Materials*, 2020, 8(9): 1901885.
- [14] Zheng P C, Zhu Z X, Pei X C, et al. Compound super-oscillation lens for reflective confocal imaging[J]. *Optics and Lasers in Engineering*, 2023, 166: 107572.
- [15] Gao Y, Liu K, Sun Z Y, et al. Beam shaping with vortex beam generated by liquid crystal spatial light modulator[J]. *Proceedings of SPIE*, 2015, 9446: 94463Z.
- [16] Khonina S N, Porfirev A P. Clusters of rotating beams with autofocusing and transformation properties generated by a spatial light modulator[J]. *Applied Physics B*, 2023, 129(4): 50.
- [17] 朱妍, 张锦, 蒋世磊, 等. 新型  $5 \times 5$  分束相位型达曼光栅的设计[J]. *激光与光电子学进展*, 2022, 59(13): 1305002.  
Zhu Y, Zhang J, Jiang S L, et al. Design of novel type of  $5 \times 5$  beam splitting phase dammann grating[J]. *Laser & Optoelectronics Progress*, 2022, 59(13): 1305002.
- [18] Xu N, Liu G X, Kong Z, et al. Creation of super-resolution hollow beams with long depth of focus using binary optics[J]. *Applied Physics Express*, 2020, 13(1): 012003.
- [19] 夏小兰, 曾宪智, 宋世超, 等. 基于柱矢量光调控的纵向超分辨率准球形多焦点阵列[J]. *光电工程*, 2022, 49(11): 220109.  
Xia X L, Zeng X Z, Song S C, et al. Longitudinal super-resolution spherical multi-focus array based on column vector light modulation[J]. *Opto-Electronic Engineering*, 2022, 49(11): 220109.
- [20] Wu Z X, Li X Y, Zou Y Y, et al. Sub-diffraction metalens for generating longitudinal bifoci and optical needles[J]. *Journal of the Optical Society of America B*, 2023, 41(1): 159-165.
- [21] Goodman J W. *Introduction to Fourier optics*[M]. 3rd ed. Englewood: Roberts & Co., 2005.
- [22] 陈刚, 温中泉, 武志翔. 光学超振荡与超振荡光学器件[J]. *物理学报*, 2017, 66(14): 144205.  
Chen G, Wen Z Q, Wu Z X. Optical super-oscillation and super-oscillatory optical devices[J]. *Acta Physica Sinica*, 2017, 66(14): 144205.
- [23] Strutt J W. *On the theory of optical images, with special reference to the microscope*[M]//Scientific papers. Cambridge: Cambridge University Press, 2009: 118-125.

## Construction of Far-Field Super-Resolution Optical Field Based on Spatial Light Modulator

Li Xinyu<sup>1</sup>, Huang Ziwen<sup>2</sup>, Zhao Changdong<sup>1</sup>, Zou Yiyang<sup>2</sup>, Li Zhanfeng<sup>1</sup>, Shang Liping<sup>2,3</sup>,  
Deng Hu<sup>2</sup>, Wu Zhixiang<sup>2\*</sup>

<sup>1</sup>*School of Manufacturing Science and Engineering, Southwest University of Science and Technology, Mianyang 621010, Sichuan, China;*

<sup>2</sup>*School of Information Engineering, Southwest University of Science and Technology, Mianyang 621010, Sichuan, China;*

<sup>3</sup>*Joint Lab Extreme Condit Matter Properties, Southwest University of Science and Technology, Mianyang 621010, Sichuan, China*

### Abstract

**Objective** The traditional focusing device is restricted by the Abbe diffraction limit. This means that the spatial resolution cannot exceed its theoretical minimum value of  $0.5\lambda/NA$ , where  $\lambda$  is the working wavelength and  $NA$  is the numerical aperture. Existing methods to break the diffraction limit require a near-field environment, which is insufficient for far-field super-resolution imaging in the optical sense. The principle of optical super-oscillation states that it is theoretically possible to produce a super-resolution spot of arbitrary smallness by rationally modulating the wavefront of incident light. Optical super-oscillation has been extensively studied by researchers in super-resolution optical lenses, and this principle enables the experimental realization of far-field super-resolution focusing. However, the optical field regulation of the super-oscillation lens depends on precise nano-processing technology. Additionally, the fabrication cost and complexity limit the device to a small size. Thus, we propose a method to generate the far-field super-resolution optical field based on the spatial light modulator. The design of the far-field super-resolution focusing device is based on the super-oscillation principle, with the binary particle swarm optimization algorithm and the angular spectrum diffraction theory combined. The generated focal spot full width at half maximum (FWHM) is smaller than the diffraction limit, which can be employed to construct the far-field super-resolution optical field.

**Methods** The device is designed based on the super-oscillation principle and adopts eight-value phase control for circularly polarized light with a wavelength of 632.8 nm. The two-dimensional phase distribution of the device is optimized using the binary particle swarm optimization algorithm and angular spectrum diffraction theory. This optimization helps obtain the optimal phase of the mask and its corresponding characteristic parameters. The device is composed of a series of concentric ring belts, each with 8  $\mu\text{m}$  width, which is equal to the size of spatial light modulator (SLM) pixels adopted in subsequent experiments. To obtain an optimized phase mask, we calculate the phase of each ring belt and generate a grayscale image based on the SLM phase control characteristics. Additionally, to verify the focusing performance of the designed device, we design and build a construction and measurement system for the far-field super-resolution optical field. We measure the characteristic parameters of the super-resolution optical field using an objective lens combined with a complementary metal oxide semiconductor (CMOS) camera. The motorized linear translation stage is moved to obtain the two-dimensional optical field distribution at different positions. Finally, an image processing algorithm is then utilized to extract the key focusing parameters of the focal spot, leading to a three-dimensional intensity distribution of the optical field.

**Results and Discussions** First, the corresponding grayscale images are generated based on the phase of each ring belt of the super-oscillatory mask obtained from the optimized design (Fig. 3). Next, the design results of the optical field are calculated by adopting the angular spectrum diffraction theory (Fig. 4). An experimental platform is then set up, and the super-oscillatory mask is loaded onto the liquid crystal screen of the spatial light modulator. Finally, the optical field is scanned and tested within the range of  $Z=185.00$  mm to  $Z=195.00$  mm. The scanning step  $\Delta Z$  is 0.05 mm, and the intensity distribution of the optical field is obtained. Experiment and theoretical results demonstrate excellent agreement, and the transverse FWHM at the focal length of the focal spot is 22.384  $\mu\text{m}$ , which is below the diffraction limit ( $0.5\lambda/NA$ , 23.732  $\mu\text{m}$ ), with far-field super-resolution focusing achieved (Fig. 6). Along the propagation direction, the vertical FWHM is 6.029 mm, creating an optical needle (Fig. 7). The device is easy to operate and does not require complex processing.

**Conclusions** To solve the problem of traditional focusing devices are constrained by the diffraction limit, we propose a method for constructing a far-field super-resolution optical field with eight-value phase control based on the optical super-oscillation principle. By adopting particle swarm optimization and angular spectrum diffraction theory, we design a far-field super-resolution focusing device for circularly polarized light with a wavelength of 632.8 nm. This is achieved by loading a super-oscillation phase mask onto the liquid crystal screen of a spatial optical modulator. By adjusting the phase of the incident optical field, the device generates an optical needle with the vertical FWHM of 6.029 mm. The FWHM at the focal length of the focal spot is lower than the diffraction limit, thus achieving far-field super-resolution focusing. This method can be applied to the visible bands and extended to other optical bands, providing core focusing devices for optical microscopy, optical imaging, and other optical applications.

**Key words** physical optics; spatial light modulator; optical super-oscillation; far-field super-resolution focusing; angular spectrum diffraction; optical field measurement